RSC Advances

PAPER

View Article Online
View Journal | View Issue

Cite this: *RSC Adv.*, 2015, **5**, 56526

Nature of defects in blue light emitting $CaZrO_3$: spectroscopic and theoretical study

Santosh K. Gupta,*[a] P. S. Ghosh,[b] N. Pathak[a] and R. Tewari[b]

The optical behaviour of a perovskite ceramic $CaZrO_3$ is investigated. The orthorhombic $CaZrO_3$ was obtained by gel combustion synthesis which yielded phase pure product at temperatures as low as 600°C. Transmission electron microscopy shows the formation of highly monodisperse nanospheres of calcium zirconate. Despite the absence of any activator, undoped $CaZrO_3$ showed distinct excitation and emission spectra attributed to the presence of local defects in the perovskite phase. Photoluminescence decay and EPR spectroscopy shows the presence of oxygen vacancies which is responsible for intense violet blue emission in the $CaZrO_3$ nanospheres. The presence of oxygen vacancies was further confirmed by comparing the intensity of emission and the EPR spectrum of the sample annealed in completely reducing and completely oxidizing atmospheres with that of the as prepared sample. To explain the PL emission in the blue region, a distortion model is proposed. Our DFT based hybrid functional calculations show distortion in the Ca network causes less disorder in the unit-cell compared to the Zr network. DFT calculations also show distortion in the Ca network comprising $[CaO_7 \cdot V_O^{\cdot\cdot}]$ and $[CaO_7 \cdot V_O^{\cdot}]$ complex clusters generates shallow defect states very close to valence band maxima leading to PL emission in the blue region.

Received 22nd May 2015
Accepted 19th June 2015

DOI: 10.1039/c5ra09637e

www.rsc.org/advances

1 Introduction

A luminescence material generally emits in the visible region of the electromagnetic spectrum but they can also emit in the ultraviolet (UV) and infrared (IR) regions depending upon the activator ion doped; Gd^{3+} doped inorganic material generally emits in the UV region[1] whereas Nd, Yb, Er doped ones emit in the IR region.[2,3] In general phosphors are classified into two main groups: activator and non-activator based phosphor materials.[4] Activator based luminescence materials generally involves transitions between energy level of activator ion like $GdPO_4$:Eu,[5] K_2TiF_6:Mn,[6] $Bi_2(Ga,Al)_4O_9$:Cr,[7] α-GdB_5O_9:Ce^{3+}/Tb^{3+} [8] *etc.* However in some cases even without activator ion; luminescence is observed which is mainly because of intrinsic charge transfer transition like in Sr_2CeO_4, $AMoO_4$ (A = Ca, Sr and Ba), $CaWO_4$ *etc.*[9–11] Rare earth doped luminescence materials in most cases are very expensive and non-environmentally benign. Other class of luminescence materials is semiconductors and defect based inorganic compounds. However many semiconductors possess intrinsic hazard and also some of them are potential threat to environment and that's why their usage is very limited.[4] As far as defect induced emission in inorganic material is concerned it has been explored long back in 1986 and later in 1997. Sailor and group has found intense white emission from silicate–carboxylate precursor.[12,13] From then onward defect related emission without any activator ion has been the emerging area of research and lots of attention has been given on how to replace traditional phosphor by rare earth free one. In that way defect based luminescence materials has contributing significantly. Some of the recent work where defect induced emission has been explored is Zn_2GeO_4,[14] InGaAs quantum dots,[15] silicon nitride,[16] ThO_2,[17] $MgAl_2O_4$,[18] CdSe nanocrystals[19] *etc.*

In this context ceramic oxide with perovskite structure has gained lots of attention particularly the one with distorted structure.

Lots of reports are available on the existence of defect induced photoluminescence in ABO_3 perovskite structure like strontium titanate,[20] lead zirconate,[21] barium zirconate,[22] lead titanate,[23] calcium titanate,[24] magnesium titanate,[25] strontium zirconate[26–29] *etc.*

$CaZrO_3$ also belongs to a class of disordered perovskite with orthorhombic structure with 8 and 6-coordination for Ca and Zr respectively.[30] They are technologically important compound which finds application in diverse area of science and technology like, Hydrogen sensor,[31] luminescence host,[30] multilayer capacitor,[32] catalysis[33] *etc.*

As far as luminescence is concerned maximum reports exists on optical properties of Eu doped $CaZrO_3$ sample.[30,34–38] Few reports are also available on photoluminescence properties of $CaZrO_3$:Pr,[39,40] $CaZrO_3$:Tb^{3+},[41] $CaZrO_3$:Tm^{3+} [42] *etc.* As far as

[a]*Radiochemistry Division, Bhabha Atomic Research Centre, Trombay, Mumbai-400085, India. E-mail: santufrnd@gmail.com; Fax: +91-22-25505151; Tel: +91-22-25590636*

[b]*Materials Science Division, Bhabha Atomic Research Centre, Trombay, Mumbai-400085, India*

optical spectroscopy of undoped $CaZrO_3$ is concerned; not much work has been done. Recently Liu *et al.* and his group has investigated photoluminescence (PL) properties of undoped $CaZrO_3$ and attributed the intense violet-blue emission to defect cluster.[43]

Finding the origin of defect induced emission solely from PL spectroscopy will not give the true picture of the situation. So, in this study we adopt two pronged route by combining PL spectroscopy and density functional theory (DFT) based calculation to explain origin of blue emission in calcium zirconate. In one hand, we synthesize calcium zirconate using citric-assisted gel-combustion route and investigate its optical properties using PL spectroscopy. Origin of emission in naive sample is also investigated using EPR and emission lifetime spectroscopy. On the other hand, DFT based hybrid functional calculations are employed by proposing a distortion model to explain blue emission in calcium zirconate from quantum chemistry perspective.

2 Experimental

2.1 Sample preparation

Analytical grade chemicals of $ZrOCl_2$, $Ca(NO_3)_2$, NH_4NO_3 and citric acid ($C_6H_8O_7 \cdot H_2O$) were used as starting reagents for the synthesis of $CaZrO_3$ perovskite. Initially solution of calcium and zirconium oxychloride was prepared in quartz double distilled water (QDD). Then solution of ammonium nitrate was added to calcium nitrate solution followed by addition of zirconium oxychloride under vigorous stirring. Under the similar condition 2 M citric acid (acting as a fuel) was added to the mixed solution of Ca^{2+}, Zr^{4+} and ammonium nitrate. This resulted in the formation of an opal gel; which on subsequent heating at 100 °C for 10 h under IR lamp dries up completely. They were then subjected to heating at 300 °C for 10 min in muffle furnace which resulted in an ash-colored voluptuous mass. The ash-like substance was then calcined at 600 °C for 1 hour which resulted in formation of white powder.

2.2 Instrumentation

The phase purity of the prepared $CaZrO_3$ sample was confirmed by X-ray diffraction (XRD). The measurements were carried out on a PANalytical Xpert Pro diffractometer which was equipped with monochromatized Cu Kα radiation. Silicon was used as an external standard.

PL measurements were carried out on an Edinburgh FLS-900 unit equipped with CD-92 controller and microsecond Xe flash lamp with 10–100 Hz variable frequency as the excitation source. The spectral data analyses were done by F-900 software. The EPR spectra were recorded on a Bruker ESP-300 spectrometer operating at X-band frequency (9.5 GHz) equipped with 100 kHz field modulation and phase sensitive detection to obtain the first derivative signal. Diphenyl picrylhydrazyl (DPPH) was used for the calibration of *g*-values of paramagnetic species.

2.3 Computational methodology

Our calculations are based on density functional theory (DFT) along with projector augmented wave (PAW) potentials implemented in the Vienna *Ab initio* Simulation Package (VASP).[44,45] Perdew–Burke–Ernzerhof (PBE)[46] exchange-correlation functional were used for the generalized gradient approximations (GGA). We further applied the screened hybrid functional of Heyd, Scuseria, and Ernzerhof (HSE06) functional[47] to take into account the effects of nonlocal exchange. In this calculation, the screened exchange functional with 25% Hartree–Fock contribution and a screening length of 0.2 $Å^{-1}$ were used. The projector augmented wave (PAW) potentials[48] were used for the ion–electron interactions including the valence states of Ca (3s, 3p, 4s – 10 valence electrons), Zr (4s, 4p, 5s, 4d – 12 valence electrons) and O (2 s, 2p – 6 valence electrons). The Kohn–Sham single particle wave functions were expanded in a plane wave basis with kinetic energy cutoff 500 eV which showed the results were well converged at this cut off. For orthorhombic $CaZrO_3$ (CZO) unit-cell, optimization was carried out with respect to E_{cut} and *k*-point meshes to ensure convergence of total energy to within a precision 0.1 meV per atom. The Brillouin-zone (BZ) integrations were performed on a Monkhorst–Pack[49] *k*-point grid of 12 × 12 × 8 for CZO unit-cell. The total energy of CZO were optimized with respect to volume (or lattice parameter), b/a, c/a ratio and atomic positions. Conjugate gradient algorithms were used for the unit-cell relaxations (b/a, c/a ratio and atomic positions) until the residual forces and stress in the equilibrium geometry were of the order of 0.005 eV $Å^{-1}$ and 0.01 GPa, respectively. The final calculation of total electronic energy and density of states (DOS) were performed using the tetrahedron method with Blöchl corrections.[50]

3 Results and discussion

3.1 Phase purity: PXRD

Fig. 1a shows the XRD pattern of 600 °C annealed $CaZrO_3$ sample. The pattern matches completely with reported standard pattern number 35-0790 except a small peak at around $2\theta = 30.05°$. Small peak at 30.06° is because of $CaZr_4O_9$ and can hardly be avoided at such low calcination temperature. It is reported that $CaZr_4O_9$ co-exist with $CaZrO_3$ phase up to temperature of 1300 °C.[51,52] However, its existence is not going to have profound effect on photoluminescence properties of $CaZrO_3$ perovskite phase. The crystal structure of $CaZrO_3$ is orthorhombic with *Pnma* space group.

In the ABO_3 perovskite structure, coordination number of A is 12 and B is 6; but tilting of BO_6 octahedra reduces the coordination of A. In that cases perovskite doesn't remain in ideal cubic geometry and are referred as disordered perovskite. Fig. 1b shows the unit cell of $CaZrO_3$ which belongs to a class of disordered perovskite because of tilting of ZrO_6 octahedra w.r.t ideal cubic structure. This reduces the coordination number of A site *i.e.* Ca^{2+} from 12 to 8 in disordered $CaZrO_3$. In many optoelectronic devices, disordered insulators (Band Gap of $CaZrO_3$ is ~5.6 eV) can replace single-crystal semiconductors, particularly when cost is an important factor.

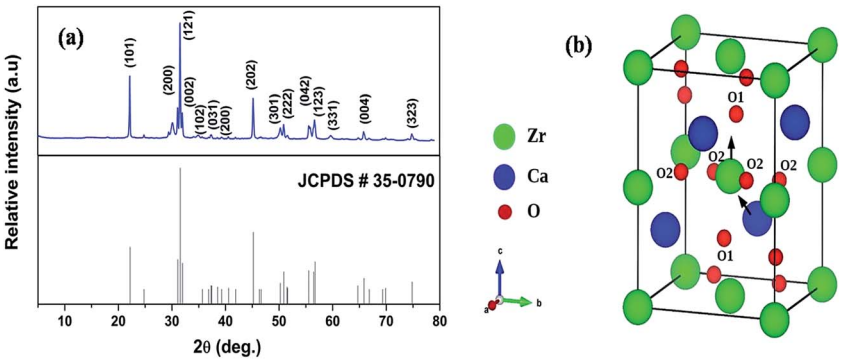

Fig. 1 (a) XRD Pattern of $CaZrO_3$ powder annealed at 600 °C (b) Schematic of $CaZrO_3$ unitcell. Arrows indicate direction of atomic displacement for the Zr and Ca network. O_1 and O_2 are the axial and planar oxygen atoms, respectively.

3.2 TEM study

Fig. 2 shows the TEM micrographs of $CaZrO_3$ nanoparticles. Fig. 2b is magnified version of one cross section of Fig. 2a. The morphologies are monodisperse sphere and similar in shapes with smooth surface. Few spheres are slightly larger compared to other. The mean diameter of the sphere is 20–30 nm.

3.3 Photoluminescence properties of undoped $CaZrO_3$

Fig. 3 shows the excitation spectra of $CaZrO_3$ sample under the emission of 427 nm. The spectra consists of a sharp peak at around 246 nm which is attributed to electron transfer from filled 2p shell of oxygen to vacant 4d shell of zirconium.[43] This is generally termed as host absorption band (HAB). Similar kind of transition is observed previously in our $SrZrO_3$ sample also.[27,28]

Fig. 4a display the emission spectrum of undoped $CaZrO_3$ sample (as prepared) at excitation wavelength of 246 nm. The emission spectrum shows a broad band at around 427 nm (visible region) in blue region of electromagnetic spectrum. CIE coordinates is very important parameter in evaluating the performance of light emitting material. CIE chromaticity diagram for $CaZrO_3$ perovskite sample is depicted in inset of Fig. 4a. The CIE coordinates value obtained in this case was found to be 0.200 and 0.196 showing $CaZrO_3$ to be a strong blue emitter. It is an important development because it is vary difficult to find a suitable blue phosphor because wide band gap is required, and the naked eye sensitivity is quite low in the blue spectral region. Such visible light emission on UV excitation in sample without any activator ion can be ascribed to presence of defects in the lattice. Liu *et al.*[43] has attributed such broad emission to $[CaO_7 \cdot V_O^{\cdot\cdot}]/[CaO_7 \cdot V_O^{\cdot\cdot}]$ defect cluster but without any experimental basis and concluded solely on work done by Longo and Group.[53,54] It is known that annealing ternary oxides at high temperature leads to creation of oxygen vacancy[55] and more likely broad blue emission in calcium zirconate is induced by oxygen vacancy.

$$O_0 = \frac{1}{2}O_2 + V_O^{\cdot\cdot} + 2e^- \quad (1)$$

To confirm that it is indeed oxygen vacancy which is responsible for intense blue emission in calcium zirconate we have annealed the as prepared sample at 800 °C in argon as well as oxygen atmosphere (pure O_2 at 1 atmospheric pressure) and their respective emission spectra is shown in Fig. 4b. It is interesting to observe that for sample annealed in oxygen atmosphere; intensity of blue emission decreases whereas it enhances in argon atmosphere compare to that of as prepared $CaZrO_3$. O_2 present in oxygen environment combines with oxygen vacancies present in thermally treated $CaZrO_3$ and that's why emission intensity decreases in completely oxygen environment. These results indicate that photoluminescence in

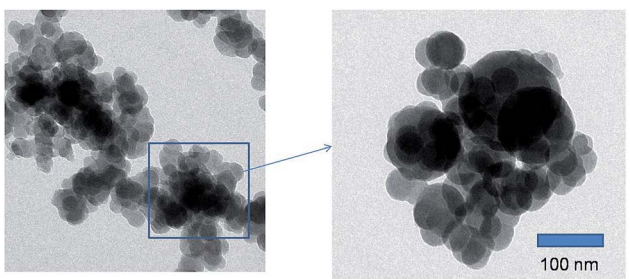

Fig. 2 (a) and (b) TEM micrographs of $CaZrO_3$ nanoparticles.

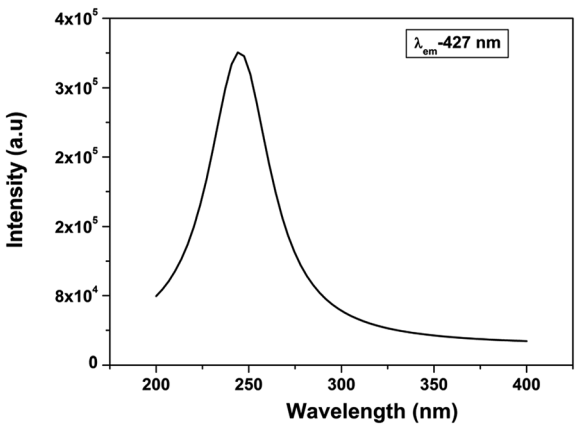

Fig. 3 Excitation spectrum of $CaZrO_3$ under λ_{em}-427 nm.

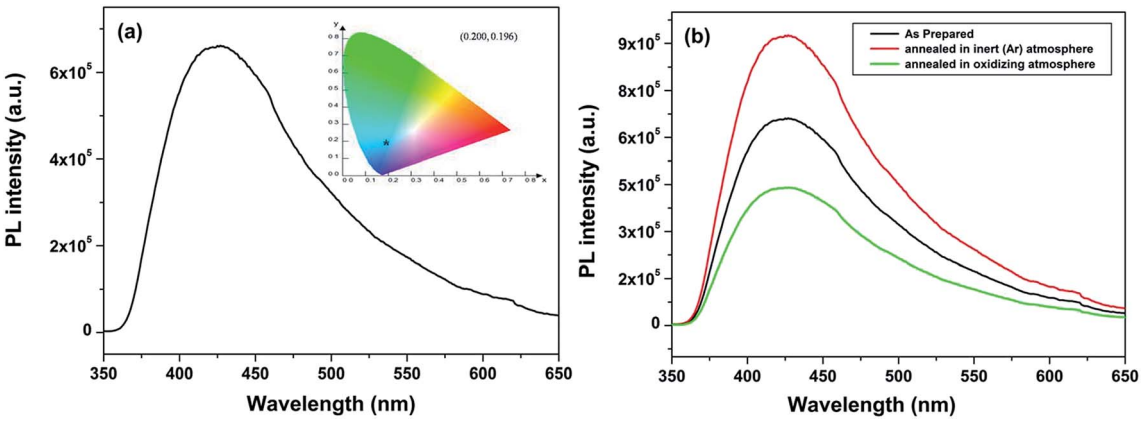

Fig. 4 (a) Emission spectrum of $CaZrO_3$ (a) as prepared and (b) sample annealed in completely oxidizing and argon atmosphere at excitation wavelength of 246 nm. CIE color coordinates for the as prepared $CaZrO_3$ sample is shown in the insets of Fig. 5a.

blue region is invariable due to oxygen vacancies. Oxygen vacancies may act as radiative centres giving rise to blue emission in $CaZrO_3$.

3.4 Probing the type of oxygen vacancy: lifetime and EPR

Since oxygen vacancy play very important part in lots of new chemical and physical processes; identifying them as well as various oxygen vacancy (OV) structures is of paramount importance for fundamental as well as from technical point of view. We have carried out emission lifetime and EPR measurement to confirm that the nature of oxygen vacancies responsible for intense blue emission in $CaZrO_3$. Normally in nanomaterials based on preparation methodology and conditions; various kinds of defects are present *viz.* cation vacancy, cation antisite, oxygen vacancy, oxygen antisite, cation interstitial, and oxygen interstitial. Even in oxygen vacancy there are three different types; neutral, singly ionized and doubly ionized depending upon the number of electron it has trapped zero, one or two.

To get detailed information about the species responsible for visible luminescence in $CaZrO_3$ sample, decay curves corresponding to blue emission from the samples were recorded and are shown in Fig. 5. The PL decay curve was fitted using bi-exponential model using equation:

$$I\ (t) = A_1 \exp\left(-\frac{t}{\tau_1}\right) + A_2 \exp\left(-\frac{t}{\tau_2}\right) \quad (2)$$

where $I(t)$ is intensity, τ_1 and τ_2 are emission decay times, and A_1 and A_2 are their relative weightage. The decay curve shows two different lifetime value 1.23 and 12.3 ns with magnitudes 87 and 13% respectively. The bi-exponential decay is an indication for the presence of more than one defect centre in $CaZrO_3$ perovskite sample. The lifetime value of the order 1.2 ns is typical of oxygen vacancy related defects[56] and the other one (12.3 ns) can be because of some surface defects which can come into picture in nanostructure materials.

Electron paramagnetic resonance (EPR) is an efficient tool for characterizing the spin state of electron and surface structure of nanomaterials. Since $CaZrO_3$ is an antimagnetic it will not have an EPR signal of its own. The fact that $CaZrO_3$ is giving an intense room temperature EPR signal (Fig. 6a) at around 3350 Gauss with $g \sim 1.9543$ which is typical of singly ionized oxygen vacancy ($V_O^{\cdot}$).[57]

Fig. 6b is showing the EPR spectra after various pretreatment of the samples at different atmospheres (inert Ar) and oxidizing atmosphere. From the figure it is clear that the intensity of the signal got modified depending on the nature of the atmosphere of pretreatment. In case of inert atmosphere pretreatment, the intensity was found to increase while a reverse result was observed in oxidizing atmosphere. The trend is very similar to what we have observed for emission spectra. Hence the EPR signal is closely related to oxygen vacancies since the emission observed in the visible region is due to oxygen vacancies. As in present case we did not observed any doublet (fine structure) for typical $S = 1$ system, the possible involvement of two trapped electrons defects $V_O^{\cdot\cdot}$ has been removed from our consideration. Hence the signal is attributed to the paramagnetic singly ionized oxygen vacancy ($V_O^{\cdot}$).[27,28]

3.5 DFT calculations

$CaZrO_3$ (CZO) crystallizes in the orthorhombic crystal structure (*Pbnm* space group) in which the atoms occupy Wycoff's

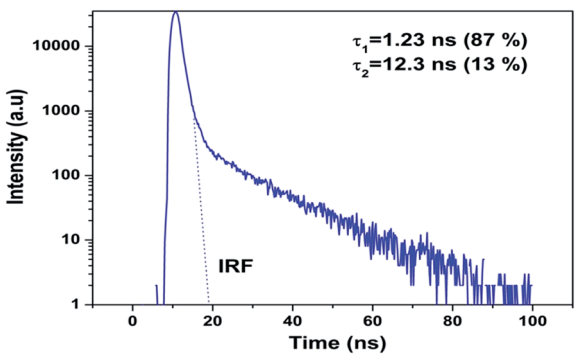

Fig. 5 PL decay profile for $CaZrO_3$ under excitation of 246 nm and emission of 427 nm. Line at $t = 0$ represents an instrumental response function (IRF).

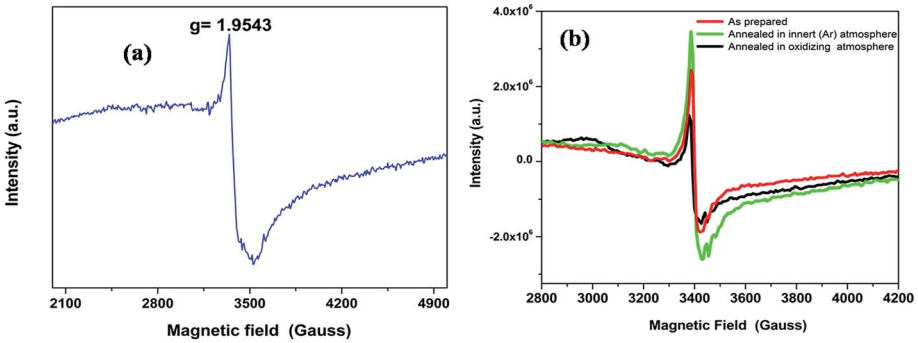

Fig. 6 (a) The EPR spectra of the $CaZrO_3$ at room temperature and (b) The EPR spectra of the $CaZrO_3$ annealed at different atmosphere.

positions: Ca (4c) (x, 1/4, z), Zr (4b) (1/2, 0, 0), O (4c) (x, 1/4, z) and O (8d) (x, y, z). Fig. 1b shows unit-cell of the $CaZrO_3$. The equilibrium lattice parameters and atomic positions are summarized in Table 1 along with experimentally determined those values (by Rietveld refinements). Table 1 clearly shows our HSE06 calculated values agree well with previous experimentally determined values[58,59] within less than 1.5% deviations.

The HSE06 calculated total and orbital angular momentum resolved electronic density of states (DOS) of CZO is shown in Fig. 7. The DOS of CZO essentially illustrates the bottom of the conduction band mainly stems from the hybridization of 4s-3d states of Ca and 4d states of Zr. The top of the valence band is mainly composed of the 2p (p_x, p_y, p_z) atomic orbital of O along with partly derived from 4d (mainly d_{xz}, d_{xy}, d_{yz}) atomic orbitals of Zr. This DOS features indicates that the host absorption of CZO originates mainly from the charge transfer from O^{2-} to Zr^{4+}. It is also important to note that, the Zr–O bond is partly covalent while the Ca–O bond is ionic in nature. The ionic bond between Ca and O indicates that electron transfer from O^{2-} to Ca^{2+} is difficult. Finally, our HSE06 calculated electronic band gap of 5.6 is matching very well with previously UV-visible spectroscopy measured band-gap of 5.7 (ref. 59) and 5.53 eV.[43]

In order to simulate the disordered types and structural complex vacancies associated with them which can explain photo-luminescence properties of CZO, three structural models were built based on the ideal/ordered CZO unit-cell (o-CZO) (i) by displacement of the Zr (f-CZO); (ii) by displacement of Ca (m-CZO); and (iii) by simultaneous displacement Zr/Ca (fm-CZO) as described by V. M. Longo *et al.*[60] Fig. 1b shows the direction of Ca and Zr atom displacements with displacement vector of (0.35 0.0 0.35) and (0.0 0.0 0.5) in Å, respectively. O_1 and O_2 are the axial and planar oxygen atoms, respectively, associated with the displaced Zr atom. The DOS were calculated with the total 0.5 Å vector displacement of the Zr and Ca network in all the disordered/distortion models. In CZO unit-cell Zr atom is coordinated by 6 nearest neighbour O atoms forming ZrO_6 octahedra. Shifting a Zr atom (situated at (0.5, 0.5, 0.5) atomic position) from its previous position causes asymmetries in the unit-cell and the shifted Zr atom is now surrounded by 5 O atoms in square base pyramid configuration. This asymmetry in the f-CZO model gives rise to complex cluster

Table 1 HSE06 calculated equilibrium lattice parameters, atomic positions and band-gap are summarized in this table along with previous experimental measurements

	This study (HSE06)	Experiment[58]	Experiment[59]
a (Å)	5.6406	5.5974(3)	5.5944
b (Å)	8.1071	8.0271(1)	8.0211
c (Å)	5.8317	5.7691(4)	5.7611
Ca 4(c)			
x	0.013	0.0108	0.0125
z	0.051	0.0478	0.0479
O 4(c)			
x	0.609	0.5806	0.6130
z	−0.043	−0.0223	−0.0423
O 8(d)			
x	0.303	0.3002	0.2999
y	0.058	0.0459	0.0566
z	0.301	0.3069	0.3011
Band gap (eV)	5.6	—	5.7

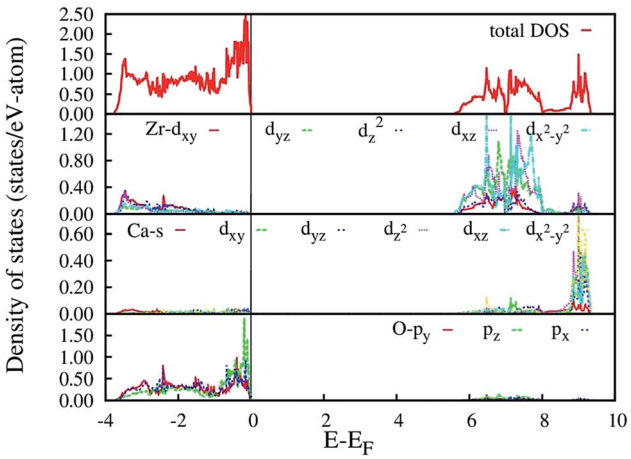

Fig. 7 HSE06 calculated total and angular momentum decomposed electronic density of states of ideal CZO (o-CZO). The vertical lines represent Fermi level.

designated as $[ZrO_6]-[ZrO_5\cdot V_O^Z]$ where $V_O^Z = V_O^\times$, $V_O^\cdot$, $V_O^{\cdot\cdot}$, depending on the displacement in the Zr atom. Similarly, shifting a Ca atom from its previous position causes asymmetries in the unit-cell and the shifted Ca atom is now surrounded by 7 O atoms while the other Ca atoms are surrounded by 8 O atoms. This asymmetry in the m-CZO model gives rise to complex cluster designated as $[CaO_8]-[CaO_7\cdot V_O^Z]$.

The calculated total and orbital angular momentum resolved DOS for f-CZO model is shown in Fig. 8, ranging from −5 eV below the top of the VB to 10 eV above and presenting the principles orbital states which influences the gap states. As seen in Fig. 8, in the case of f-CZO, the VB is composed of O 2p states and the upper part of VB, *i.e.* the new states, is composed mainly of axial oxygen 2p states as well as planner oxygen 2p states. In the axial oxygen contribution p_z orbital and in the planner oxygen contribution p_x, p_y as well as p_z orbitals actively participate to generate defect states. New defect states in the lower part of the conduction band are generated mostly by the Zr-$d_{x^2-y^2}$ atomic orbitals. In the m-CZO model (Fig. 9), the upper part of VB, *i.e.* the new states, is composed mainly of planner oxygen 2p states as well as axial oxygen 2p states. In the planner oxygen contribution p_z orbital and in the axial oxygen contribution p_x, p_y as well as p_z orbitals actively participate to generate defect states. It is crucial to note that, the HSE06 calculated electronic band-gap is 4.73 and 4.98 eV for f-CZO and m-CZO disordered model, respectively.

Based on our disordered model and DFT calculations, it is clear that the displacement in network former (f-CZO model) causes increased degree of disorder in the lattice compared to the network modifier (m-CZO model). The degree of disorder is characterized by the reduction in the electronic band-gap energy in the disordered model.[60] The HSE06 calculated electronic band-gap energies of dislocation model structures follow the same sequence in which degree of disorder is present in these model structures. The decrease in band gap in structurally disordered powder can be attributed to local defects and/or

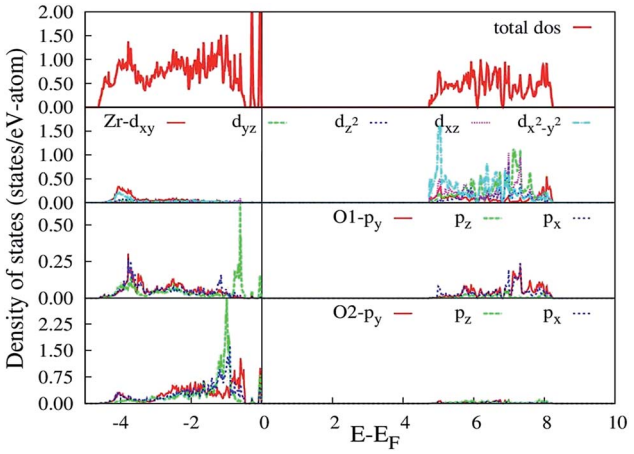

Fig. 8 HSE06 calculated total and angular momentum decomposed electronic density of states of f-CZO distortion model. The vertical lines represent Fermi level. O_1 and O_2 correspond to axial and planar oxygen atoms, respectively.

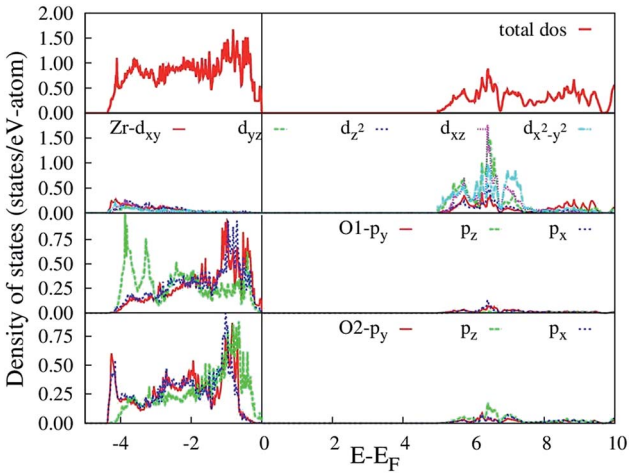

Fig. 9 HSE06 calculated total and angular momentum decomposed electronic density of states of m-CZO distortion model. The vertical lines represent Fermi level. O_1 and O_2 correspond to axial and planar oxygen atoms, respectively.

local bond distortion, which gives rise to defect electronic levels in the band gap of this material. Increased disorder is linked to deep defects inserted in the band-gap and increased order is associated with shallow defects, which disappear when degree of disorder is less. Increased disorder is due to presence of $[ZrO_5\cdot V_O^{\cdot\cdot}]$ and $[ZrO_5\cdot V_O^{\cdot}]$ complex clusters and are deeply inserted in the band-gap, leading to orange–red PL emission. $[CaO_7\cdot V_O^{\cdot\cdot}]$ and $[CaO_7\cdot V_O^{\cdot}]$ complex clusters are linked to shallow defects in the band-gap and lead to a more energetic PL emission (violet–blue light).[60] The deep defects linked to the Zr disorder are associated with the 2p states of axial oxygens and evidently shown in Fig. 9. The shallow defects can be ascribed to the 2p states of planar oxygen in the upper part of valence band as described in Fig. 9.

The emission spectrum of CZO is a broad band covering visible spectra from ~370 nm to 650 nm (Fig. 4a). But the intensity of the spectrum is very high in the blue region. Moreover, our DFT based hybrid-functional calculations on the m-CZO distortion model shows generation of shallow defect states leads to PL emission in the violet-blue region. Therefore, shallow defect states comprising $[CaO_7\cdot V_O^{\cdot\cdot}]$ and $[CaO_7\cdot V_O^{\cdot}]$ complex clusters gives maximum contribution in the blue region PL emission. Increasing the lattice order causes these complex vacancies and the PL emission to disappear. The presence of oxygen vacancy is also confirmed by EPR studies as discussed in Section 3.4.

4 Conclusion

Pure orthorhombic phase of distorted $CaZrO_3$ perovskite is synthesized using gel-combustion route at 600 °C. The phase purity of the sample is confirmed by X-ray diffraction (XRD). Transmission electron microscopy of the sample shows the spherical morphology of CZO nanocrystal with particle size in the range 30–40 nm. On irradiating the CZO nanosphere with UV light it is showing an intense violet-blue emission without

the presence any activator ion. It is interesting to observe that for sample annealed in oxygen atmosphere; intensity of blue emission decreases whereas it enhances in argon atmosphere compare to that of as prepared $CaZrO_3$. The bi-exponential PL decay was observed for CZO sample which is an indication for the presence of more than one defect centre in $CaZrO_3$ perovskite sample. The lifetime value of the order 1.2 ns is typical of oxygen vacancy related defects and the other one (12.3 ns) can be because of some surface defects. The presence of oxygen vacancy in CZO nanostructure was further confirmed by EPR spectroscopy which gives an intense signal $g \sim 1.9543$ which is typical of singly ionized oxygen vacancy ($V_O^{\cdot}$). To explain PL emission in the blue region, a distortion model is proposed where distortion is given in Ca and Zr atom network separately. Our DFT based hybrid functional calculations shows distortion in Ca network causes less disorder in unit-cell compared to Zr network. DFT calculations also shows distortion in Ca network (m-CZO model) comprising of $[CaO_7 \cdot V_O^{\cdot\cdot}]$ and $[CaO_7 \cdot V_O^{\cdot}]$ complex clusters generates shallow defect states (localized very close to valence band maxima) reduce the band-gap energies. Similarly, distortion in Zr network (f-CZO model) comprising $[ZrO_5 \cdot V_O^{\cdot\cdot}]$ and $[ZrO_5 \cdot V_O^{\cdot}]$ complex clusters generates deep defect states. When structural order increases the band-gap energies are also increased by confirming the fact that PL is directly associated with the localized states exists in the band-gap region. Moreover, shallow defect states comprising of $[CaO_7 \cdot V_O^{\cdot\cdot}]$ and $[CaO_7 \cdot V_O^{\cdot}]$ complex clusters gives maximum contribution in the blue region PL emission. Increasing the lattice order causes these complex vacancies and the PL emission to disappear. The presence of oxygen vacancy is also confirmed by EPR studies.

References

1 S. K. Gupta, R. M. Kadam, V. Natarajan and S. V. Godbole, *Mater. Sci. Eng., B*, 2014, **183**, 6.
2 M. K. Ekmecki, M. Erdem and A. S. Basak, *Dalton Trans.*, 2015, **44**, 5379.
3 L. Sun, Y. Qiu, T. Liu, H. Zhang and L. Shi, *ACS Appl. Mater. Interfaces*, 2013, **5**, 9585.
4 C. Zhang and J. Lin, *Chem. Soc. Rev.*, 2012, **41**, 7938.
5 Q. Du, Z. Huang, Z. Wu, X. Meng, G. Yin, F. Gao and L. Wang, *Dalton Trans.*, 2015, **44**, 3934.
6 L. Lv, Z. Chen, G. Liu, S. Huang and Y. Pan, *J. Mater. Chem. C*, 2015, **3**, 1935.
7 C. Liu, Z. Xia, M. Chen, M. S. Molokeev and Q. Liu, *Inorg. Chem.*, 2015, **54**, 1876.
8 X. Sun, W. Gao, T. Yang and R. Cong, *Dalton Trans.*, 2015, **44**, 2276.
9 S. K. Gupta, M. Sahu, K. Krishnan, M. Saxena, V. Natarajan and S. V. Godbole, *J. Mater. Chem. C*, 2013, **1**, 7054.
10 P. Jena, S. K. Gupta, V. Natarajan, O. Padmaraj and N. Satyanarayana, *Mater. Res. Bull.*, 2015, **64**, 223.
11 J. Janbua, J. Mayamae, S. Wirunchit, R. Baitahe and N. Vittayakorn, *RSC Adv.*, 2015, **5**, 19893.
12 S. Angelov, R. Stoyanova, R. Dafinova and K. Kabasanov, *J. Phys. Chem. Solids*, 1986, **47**, 409.
13 W. H. Green, K. P. Le, J. Grey, T. T. Au and M. J. Sailor, *Science*, 1997, **276**, 1826.
14 Z. Y. Xie, H. L. Lu, Y. Zhang, Q. Q. Sun, P. Zhou, S. J. Ding and D. W. Jhang, *J. Alloys Compd.*, 2015, **619**, 368.
15 F. Hu, Z. Cao, C. Zhang, X. Wang and M. Xiao, *Sci. Rep.*, 2015, **5**, 8898.
16 W. Zhu, B. McEntire, Y. Enomoto, M. Boffelli and G. Pezz, *J. Phys. Chem. C*, 2015, **119**, 3279.
17 S. K. Gupta, P. S. Ghosh, A. Arya and V. Natarajan, *RSC Adv.*, 2014, **4**, 51244.
18 S. K. Gupta, V. Grover, K. P. Muthe, V. Natarajan and A. K. Tyagi, *J. Mol. Struct.*, 2015, **1089**, 81.
19 Y. F. Lu and X. A. Cao, *Appl. Phys. Lett.*, 2014, **105**, 203101.
20 A. E. Souza, G. T. A. Santos, B. C. Barra, W. D. Macedo, S. R. Teixeira, C. M. Santos, A. M. O. R. Senos, L. Amaral and E. Longo, *Cryst. Growth Des.*, 2012, **12**, 5671.
21 J. M. A. Nunes, J. W. M. Espinosa, M. F. C. Gurgel, P. S. Pizani, S. H. Leal, M. R. M. C. Santos and E. Longo, *Ceram. Int.*, 2012, **38**, 4593.
22 S. Parida, S. K. Rout, L. S. Cavalcante, E. Sinha, M. S. Li, V. Subramanian, N. Gupta, V. R. Gupta, J. A. Varela and E. Longo, *Ceram. Int.*, 2012, **38**, 2129.
23 R. I. Eglitis, E. A. Kotomin, V. A. Trepakov, S. E. Kapphan and G. Borstel, *J. Phys.: Condens. Matter*, 2002, **14**, L647–L653.
24 M. L. Moreira, E. C. Paris, G. S. do Nascimento, V. M. Longo, J. R. Sambrano, V. R. Mastelaro, M. I. B. Bernardi, J. Andrés, J. A. Varela and E. Longo, *Acta Mater.*, 2009, **57**, 2174.
25 E. A. V. Ferri, J. C. Sczancoski, L. S. Cavalcante, E. C. Paris, J. W. M. Espinosa, A. T. de Figueiredo, P. S. Pizani, V. R. Mastelaro, J. A. Varela and E. Longo, *Mater. Chem. Phys.*, 2009, **117**, 192.
26 V. M. Longo, L. S. Cavalcante, R. Erlo, V. R. Mastelaro, A. T. De Figueiredo, J. R. Sambrano, S. de Lazaro, A. Z. Freitas, L. Gomes, N. D. Vieira Jr, J. A. Varela and E. Longo, *Acta Mater.*, 2008, **56**, 2191.
27 S. K. Gupta, P. S. Ghosh, N. Pathak, A. Arya and V. Natarajan, *RSC Adv.*, 2014, **4**, 29202.
28 N. Pathak, S. K. Gupta, P. S. Ghosh, A. Arya, V. Natarajan and R. M. Kadam, *RSC Adv.*, 2015, **5**, 17501.
29 V. M. Longo, L. S. Cavalcante, A. T. De Figueiredo, L. P. S. Santos, E. Longo, J. A. Varela, J. R. Sambrano and A. C. Hernandes, *Appl. Phys. Lett.*, 2007, **90**, 091906.
30 S. Sakaida, Y. Shimokawa, T. Asaka, S. Honda and Y. Iwamoto, *Mater. Res. Bull.*, 2015, **67**, 146.
31 M. S. Islam, R. A. Davies and J. D. Gale, *Chem. Mater.*, 2001, **13**, 2049.
32 M. Pollet and S. Marinel, *J. Mater. Sci.*, 2004, **39**, 1943.
33 H. Wang, M. Wang, W. Zhang, N. Zhao, W. Wei and Y. Sun, *Catal. Today*, 2006, **15**, 107.
34 Y. Shimokawa, S. Sakaida, S. Iwata, K. Inoue, S. Honda and Y. Iwamoto, *J. Lumin.*, 2014, **157**, 113.
35 Sheetal, V. B. Taxak, S. Singh, Mandeep and S. P. Khatkar, *Optik*, 2014, **125**, 6340.
36 Q. Du, G. Zhou, J. Zhou and H. Zhou, *J. Lumin.*, 2013, **137**, 83.
37 J. Huang, L. Zhou, Y. Lan, F. Gong, Q. Li and J. Sun, *Cent. Eur. J. Phys.*, 2011, **9**, 975.

38 H. Zhang, X. Fu, S. Niu and Q. Xin, *J. Alloys Compd.*, 2008, **459**, 103.
39 E. Pinel, P. Boutinaud and R. Mahiou, *J. Alloys Compd.*, 2004, **380**, 225.
40 Z. Liu, Y. Liu, J. Zhang, J. Rong, L. Huang and D. Yuan, *Opt. Commun.*, 2005, **251**, 388–392.
41 V. Singh, A. Watanabe, T. K. Gundu Rao, K. Al-Shamery, M. Haase and Y. D. Jho, *J. Lumin.*, 2012, **132**, 2036.
42 H. Zhang, X. Fu, S. Niu and Q. Xin, *J. Lumin.*, 2008, **128**, 1348.
43 X. Liu, J. Zhang, X. Ma, H. Sheng, P. Feng, L. Shi, R. Hu and Y. Wang, *J. Alloys Compd.*, 2013, **550**, 451.
44 G. Kresse and J. Furthmueller, *Phys. Rev. B: Condens. Matter Mater. Phys.*, 1996, **5**, 11169.
45 G. Kresse and J. Furthmueller, *Comput. Mater. Sci.*, 1996, **6**, 15.
46 J. P. Perdew, K. Burke and M. Ernzerhof, *Phys. Rev. Lett.*, 1996, **77**, 3685.
47 M. Marsman, J. Paier, A. Stroppa and G. Kresse, *J. Phys.: Condens. Matter*, 2008, **20**, 064201–064202.
48 P. E. Blöchl, *Phys. Rev. B: Condens. Matter Mater. Phys.*, 1994, **50**, 17953.
49 H. J. Monkhorst and J. D. Pack, *Phys. Rev. B: Condens. Matter Mater. Phys.*, 1979, **13**, 5188.
50 P. E. Blöchl, O. Jepsen and O. K. Andesen, *Phys. Rev. B: Condens. Matter Mater. Phys.*, 1994, **4**, 16223.
51 T. Yu, C. H. Chen, Y. K. Lu, X. F. Chen, W. Zhu and R. G. Krishnan, *J. Electroceram.*, 2007, **18**, 149.
52 W. S. Lee, C. Y. Su, Y. C. Lee, S. P. Lin and T. Yang, *Jpn. J. Appl. Phys.*, 2006, **45**, 5853.
53 L. S. Cavalcante, J. C. Sczancoski, J. W. M. Espinosa, V. R. Mastelaro, A. Michalowicz, P. S. Pizani, F. S. De Vicente, M. S. Li, J. A. Varela and E. Longo, *J. Alloys Compd.*, 2009, **471**, 253.
54 L. S. Cavalcante, M. F. C. Gurgel, E. C. Paris, A. Z. Simoes, M. R. Joya, J. A. Varela, P. S. Pizani and E. Longo, *Acta Mater.*, 2007, **55**, 6416.
55 S. Nigam, V. Sudarsan and R. K. Vatsa, *Opt. Mater.*, 2011, **33**, 558.
56 N. S. Ham, H. S. Shim, J. H. Seo, S. Y. Kim, S. M. Park and J. K. Song, *J. Appl. Phys.*, 2010, **107**, 084306.
57 Z. L. Wang, C. K. Lin, X. M. Liu, G. Z. Li, Y. Luo, Z. W. Quan, H. P. Xiang and J. Lin, *J. Phys. Chem. B*, 2006, **110**, 9469.
58 P. Stoch, J. Szczerba, J. Lis, D. Madej and Z. Pedzich, *J. Eur. Ceram. Soc.*, 2012, **32**, 665.
59 I. L. V. Rosa, M. C. Oliveira, M. Assis, M. Ferrer, R. S. André, E. Longo and M. F. C. Gurgel, *Ceram. Int.*, 2015, **41**, 3069.
60 V. M. Longo, L. S. Cavalcante, R. Erlo, V. R. Mastelaro, A. T. De Figueiredo, J. R. Sambrano, S. de Lazaro, A. Z. Freitas, L. Gomes, N. D. Vieira Jr, J. A. Varela and E. Longo, *Acta Mater.*, 2008, **56**, 2191.